ICCFD13-2026-124

A Subface-Based Cell-Centered Finite Volume Scheme for Solving the Three-Dimensional Compressible Navier–Stokes Equations on Unstructured Grids Using Multi-point Flux Approximations

V. Delmas[*,**], R. Loubère[**] and P.-H. Maire[*]
Corresponding author: vincent.delmas@cea.fr
[*] CEA-CESTA, France. [**] Institut de Mathématiques de Bordeaux, France.

Abstract: We develop a robust and accurate subface-based, cell-centered finite volume (FV) method for solving the three-dimensional compressible Navier–Stokes equations in hypersonic conditions on unstructured grids. The inviscid part is discretized using a novel multi-point flux formulation that couples all Riemann problems around each mesh node through a local linear system, eliminating classical shock pathologies such as odd–even decoupling and carbuncle instabilities while preserving positivity of density and internal energy. The viscous and conductive fluxes are discretized within the same subface-based framework, leading to a symmetric positive definite local diffusion matrix. The method is validated on representative three-dimensional test cases including the Sedov blast and the Atmospheric Re-entry Demonstrator.

Keywords: Three-dimensional hypersonic flows, Finite Volume method, Approximate Riemann solvers, Positivity preserving, Multi-point scheme.

1. Context and motivations

This work focuses on the development of robust and accurate numerical methods for the simulation of three-dimensional hypersonic flows around complex vehicles. The flow regime under consideration corresponds to flight altitudes at which the continuum hypothesis is valid and the fluid behavior can be described by the compressible Navier–Stokes equations, expressing the conservation of mass, momentum, and energy. Hypersonic flows are hypervelocity flows, typically several times the speed of sound, and are characterized by extreme physical phenomena. These include strong detached shock waves, across which the flow variables experience abrupt discontinuities, leading to an intense conversion of kinetic energy into internal energy and, consequently, to very high temperatures. In addition, within a very thin region adjacent to the vehicle surface, known as the boundary layer, strong velocity and temperature gradients develop in the direction normal to the wall. These gradients induce significant transfers of momentum and energy toward the wall, resulting in severe aerodynamic and aerothermal loads. The accurate numerical prediction of these loads, and in particular of wall heat fluxes, remains a critical challenge for the design of thermal protection systems of hypersonic and space vehicles [1].

We aim at developing a robust and accurate subface-based, cell-centered FV method for solving the three-dimensional compressible Navier–Stokes equations in hypersonic conditions on hybrid unstructured grids. The use of unstructured meshes is essential for handling complex three-dimensional geometries, but it also imposes stringent requirements on the robustness, stability, and accuracy of the numerical discretization [2]. A major difficulty lies in the simultaneous resolution of strong curved bow shocks ahead of the vehicle and of the thin boundary layers along its surface. While sufficient numerical dissipation is required in the inviscid fluxes to stabilize shock waves, excessive dissipation may severely degrade the prediction of viscous stresses and heat transfer within the boundary layer. Balancing these conflicting requirements is one of the central objectives of this work.

Can we design a conservative, robust, entropy-stable and positivity-preserving finite volume method whose numerical flux is no longer purely face-normal and two-point, but genuinely multidimensional through a node-based multipoint construction?

2. Discretization of the Euler equations

In this first section, we discuss the discretization of the Euler equations through a subface-based finite volume formulation. We briefly recall the main ideas of the discretization, which has already been presented in [3, 4, 5].

2.1 Governing equations

The Euler system writes

$$\frac{\partial \mathbf{U}}{\partial t} + \nabla \cdot \mathbb{F}(\mathbf{U}) = \mathbf{0}, \tag{1}$$

where the vector of conservative variables is $\mathbf{U} = \left(\rho,\ \rho\mathbf{v},\ \rho e\right)^t$, with ρ the mass density, $\mathbf{v}$ the velocity, and $e = \epsilon + \frac{1}{2}\mathbf{v}\cdot\mathbf{v}$ the specific total energy. The physical flux tensor is

$$\mathbb{F}(\mathbf{U}) = \begin{pmatrix} \rho\mathbf{v}^t \\ \rho\mathbf{v}\otimes\mathbf{v} + p\,\mathbb{I}_d \\ \rho e\,\mathbf{v}^t + p\,\mathbf{v}^t \end{pmatrix}, \tag{2}$$

where the pressure p is related to the specific internal energy through the equation of state. A key identity used throughout the derivation of the schemes is the splitting of the normal flux into an advection part and a Lagrangian (pressure) part as

$$\mathbf{F}_\mathbf{n}(\mathbf{U}) = \mathbb{F}(\mathbf{U})\mathbf{n} = v_\mathbf{n}\mathbf{U} + \mathbf{L}, \qquad \mathbf{L} = \left(0,\ p\mathbf{n},\ \mathbf{0},\ pv_\mathbf{n}\right)^t. \tag{3}$$

2.2 Subface-based cell-centered finite volume formulation

Let $\Omega = \bigcup_{c\in C}\omega_c$ be the computational domain. For each cell ω_c, $\mathcal{P}(c)$ denotes the set of its nodes (vertices). Rather than splitting the cell boundary by faces as in the classical face-based FV method, we partition it by the *subfaces* attached to each node, see Figure 1 for an illustration.

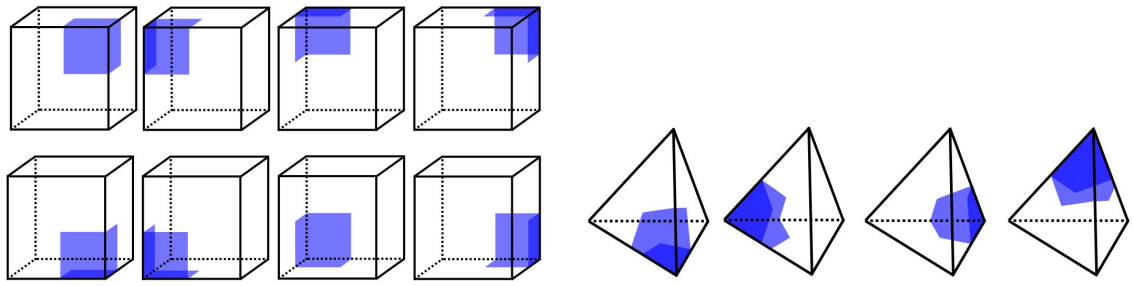

(a) Hexahedron. (b) Tetrahedron.

Figure 1: Subface partition of a face f of a cell ω_c for a tetrahedron (left) and a hexahedron (right). Each face f is split into as many subfaces as it has vertices; only one subface (shaded) is shown.

If f is a generic polygonal face with barycenter $\mathbf{x}_f$, the subface around a vertex $p \in \mathcal{P}(f)$, is created by connecting p to the midpoints of its two adjacent edges on f and to $\mathbf{x}_f$. For $p \in \mathcal{P}(c)$, the set $\mathcal{SF}(pc)$ collects the subfaces of cell c that share node p. Each subface $f \in \mathcal{SF}(pc)$ has area A_{pcf} and outward unit normal $\mathbf{n}_{pcf}$.

Integrating (1) over ω_c and using the subface decomposition yields the semi-discrete cell update

$$|\omega_c|\frac{\mathrm{d}\mathbf{U}_c}{\mathrm{d}t} + \sum_{p\in\mathcal{P}(c)}\sum_{f\in\mathcal{SF}(pc)} A_{pcf}\,\mathbf{F}_{pcf} = \mathbf{0}, \tag{4}$$

where $\mathbf{U}_c$ is the cell-averaged state and $\mathbf{F}_{pcf}$ is the flux through subface pcf. This formulation allows some freedom in achieving global conservation as we show next.

2.3 Classical and node-based conservation

We can study the conservation of the scheme by summing (4) over all cells $c \in C$, which leads to

$$\frac{\mathrm{d}}{\mathrm{d}t}\left(\sum_{c\in C}|\omega_c|\,\mathbf{U}_c\right) + \sum_{c\in C}\sum_{p\in\mathcal{P}(c)}\sum_{f\in\mathcal{SF}(pc)} A_{pcf}\,\mathbf{F}_{pcf} = \mathbf{0}. \tag{5}$$

Denoting by $\mathbf{F}^-_{pf}$ and $\mathbf{F}^+_{pf}$ the outward fluxes through subface f around node p, we can reindex the flux sum by node: each internal subface f shared between a left cell and a right cell appears exactly twice, contributing $A_{pf}\mathbf{F}^-_{pf}$ (outward from the left cell) and $-A_{pf}\mathbf{F}^+_{pf}$ (outward from the right cell, whose outward normal is $-\mathbf{n}_{pf}$). The first term in (5) is the time derivative of the total conserved quantity, which is preserved as long as boundary fluxes vanish. Hence global conservation holds if and only if

$$\sum_{p\in\mathcal{P}}\sum_{f\in\mathcal{SF}(p)} A_{pf}\left(\mathbf{F}^+_{pf} - \mathbf{F}^-_{pf}\right) = \mathbf{0}. \tag{6}$$

This leads to two local conditions for conservation. The first, Classical conservation, is the standard assumption in cell-centered FV methods. It requires the flux on each subface to be uniquely defined such that there is no jump in flux at the interface. This approach is inherently one-dimensional: each subface is treated in isolation, without any coupling to the neighboring subfaces around the same node.

Definition 1 (Classical conservation)**.**

$$\forall p \in \mathcal{P},\ \forall f \in \mathcal{SF}(p), \qquad \mathbf{F}^+_{pf} - \mathbf{F}^-_{pf} = \mathbf{0}. \tag{7}$$

The second, Node-based conservation, only requires the total flux imbalance summed over all subfaces around each node to vanish. Individual subface imbalances $\mathbf{F}^+_{pf} - \mathbf{F}^-_{pf} \neq \mathbf{0}$ are permitted, provided they cancel in the nodal sum (8). This relaxation is the key enabler of the multi-point scheme: instead of solving each subface Riemann problem independently, all Riemann problems sharing a node are solved jointly, introducing genuine multidimensional coupling directly at the discrete level.

Definition 2 (Node-based conservation)**.**

$$\forall p \in \mathcal{P}, \qquad \sum_{f\in\mathcal{SF}(p)} A_{pf}\left(\mathbf{F}^+_{pf} - \mathbf{F}^-_{pf}\right) = \mathbf{0}. \tag{8}$$

2.4 Face-conservative simple approximate Riemann solvers

Following Gallice [6] and exploiting the flux split (3) into an advection contribution and a Lagrangian (pressure) part, three face-conservative approximate Riemann solvers are derived as positivity-preserving counterparts of the HLL [7], HLLC [8], and HLLCM [9] schemes. They are referred to here as the two-wave, three-wave, and modified three-wave solvers, respectively. Their assumed wave structures are shown in Figure 2. The three solvers differ in how many intermediate states they introduce and how they are able to resolve contact waves and shear layers.

- The *two-wave* solver (Fig. 2a) has a single star state which means that it will diffuse both the contact discontinuities and the shear layers.

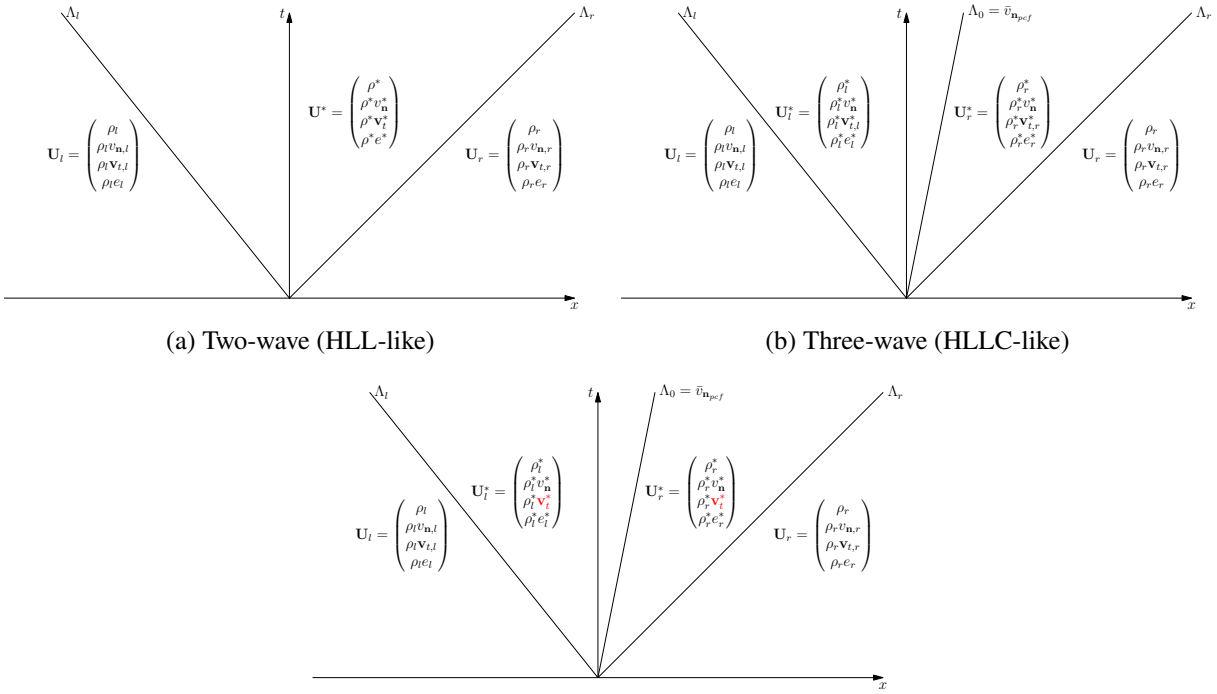

(a) Two-wave (HLL-like)

(b) Three-wave (HLLC-like)

(c) Modified three-wave (HLLCM-like)

Figure 2: Assumed intermediate states and wave speeds for the three face-conservative solvers.

- The *three-wave* solver (Fig. 2b) adds a central contact wave separating two star regions. It will preserve both the contact discontinuities and shear layers exactly (when they are aligned with the mesh and have zero relative velocity with the mesh). It is well known since [10] that it is susceptible to carbuncle-type instabilities.
- The *modified three-wave* solver (Fig. 2c) retains the three-wave structure for the density but not for the tangential velocity which gets averaged just like in the case of the *two-wave* scheme. This modification has been shown to eliminate the carbuncle-type instabilities while preserving sharp contact resolution. As we will see however, the additional viscosity introduced on shear layers will pollute the computation of the heat flux when solving the full Navier–Stokes system.

The two-wave, three-wave, and modified three-wave solvers differ from their well-known HLL, HLLC, and HLLCM counterparts in the way their wave speeds are determined. For all three solvers, the Eulerian wave speeds are systematically computed from the Lagrangian wave speeds to ensure the positivity of intermediate densities and internal energies [3]. The Lagrangian wave speeds $\lambda_l, \lambda_r > 0$ are related to the Eulerian wave speeds $\Lambda_l \leq \Lambda_r$ by

$$\Lambda_l = v_{\mathbf{n},l} - \frac{\lambda_l}{\rho_l}, \qquad \Lambda_r = v_{\mathbf{n},r} + \frac{\lambda_r}{\rho_r}. \tag{9}$$

For a convex equation of state, sufficient conditions for the positivity of the intermediate densities and internal energies are

$$\lambda_l > \max\Big(a_l\rho_l,\ -\rho_l[\![v_{\mathbf{n}}]\!],\ \sqrt{\rho_l[\![p]\!]^{(+)}}\Big), \quad \lambda_r > \max\Big(a_r\rho_r,\ -\rho_r[\![v_{\mathbf{n}}]\!],\ \sqrt{\rho_r[\![-p]\!]^{(-)}}\Big), \tag{10}$$

where a is the sound speed, $x^{(\pm)} = (|x| \pm x)/2$, and $[\![\phi]\!] = \phi_r - \phi_l$. This positivity property is the foundation of the domain-preserving CFL condition derived in [3].

2.5 Node-conservative multi-point scheme

The multi-point scheme is built on the observation that, within the subface framework, classical face-by-face conservation is not the only path to global conservation. By relaxing to node-based conservation, one gains the freedom to couple all Riemann problems around a mesh node. This coupling introduces genuine multidimensionality and eliminates the spurious pressure–velocity decoupling at the origin of carbuncle instabilities. The intermediate states share the same assumptions as the three-wave scheme:

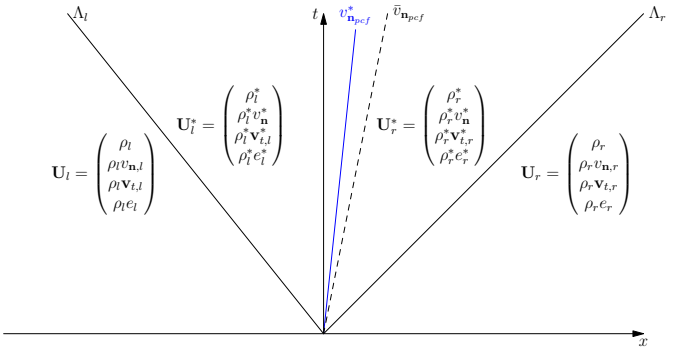

Figure 3: Multi-point scheme: the contact velocities on all subfaces around a node are projections of a single nodal velocity vector $\mathbf{v}_p$.

a single star normal velocity $v^*_{\mathbf{n}} = \Lambda_0$, left and right star densities ρ^*_l, ρ^*_r, and continuous tangential velocities. However, the left and right intermediate pressures are kept *distinct*

$$p^*_l \neq p^*_r. \tag{11}$$

With this condition, it is not possible to verify the jump relation across the central wave and as a consequence the scheme is not face-conservative. The difference between the left and right-sided fluxes can easily be computed to get

$$\mathbf{F}^+ - \mathbf{F}^- = \mathbf{L}^*_r - \mathbf{L}^*_l = (p^*_r - p^*_l) \begin{pmatrix} 0 \\ 1 \\ \mathbf{0} \\ v^*_{\mathbf{n}} \end{pmatrix}. \tag{12}$$

It can be simplified further by using the left and right jump relations to compute the intermediate pressures, which leads to

$$\mathbf{F}^+ - \mathbf{F}^- = (\lambda_l + \lambda_r)\,(v^*_{\mathbf{n}} - \bar{v}_{\mathbf{n}}) \begin{pmatrix} 0 \\ 1 \\ \mathbf{0} \\ v^*_{\mathbf{n}} \end{pmatrix}, \tag{13}$$

where $\bar{v}_{\mathbf{n}}$ is the usual Godunov velocity defined as

$$\bar{v}_{\mathbf{n}} = \frac{\lambda_r v_{\mathbf{n}_r} + \lambda_l v_{\mathbf{n}_l}}{\lambda_r + \lambda_l} - \frac{p_r - p_l}{\lambda_r + \lambda_l}. \tag{14}$$

The obvious choice $v^*_{\mathbf{n}} = \bar{v}_{\mathbf{n}}$ recovers the face-conservative three-wave scheme. The multi-point scheme instead selects $v^*_{\mathbf{n}}$ to enforce the node-based conservation.

2.5.1 Nodal velocity system

The central hypothesis of the multi-point scheme is that the normal contact velocities on all subfaces around a node are projections of a single nodal velocity vector $\mathbf{v}_p$

$$v^*_{\mathbf{n},pf} = \mathbf{v}_p \cdot \mathbf{n}_{pf}, \qquad \forall f \in \mathcal{SF}(p). \tag{15}$$

Substituting (13) and (15) into the node-based conservation condition yields the $d \times d$ linear system at each node p

$$\mathbb{M}_p \, \mathbf{v}_p = \mathbf{R}_p, \tag{16}$$

with

$$\mathbb{M}_p = \sum_{f \in \mathcal{SF}(p)} A_{pf} \, (\lambda_l + \lambda_r)_{pf} \, (\mathbf{n}_{pf} \otimes \mathbf{n}_{pf}), \tag{17}$$

$$\mathbf{R}_p = \sum_{f \in \mathcal{SF}(p)} A_{pf} \, (\lambda_l + \lambda_r)_{pf} \, \bar{v}_{\mathbf{n},pf} \, \mathbf{n}_{pf}. \tag{18}$$

The matrix $\mathbb{M}_p$ is symmetric positive definite on non-degenerate meshes, so (16) has a unique solution. Once $\mathbf{v}_p$ is known, projecting it onto every subface normal around p gives all contact velocities $v^*_{\mathbf{n},pf}$ and the complete state of every Riemann problem around node p can be computed by applying the jump relations across the left and right waves. Just as in the case of the face-conservative solvers, the Eulerian wavespeeds are determined from the Lagrangian ones to ensure the positivity of the intermediate densities and internal energies, see [4] for the full derivation.

It is worth noting that the expression of the nodal velocity is exactly the same as that obtained in the derivation of cell-centered finite-volume schemes for the Euler equations written in Lagrangian form [11]. In the Lagrangian setting, this nodal velocity is used to move the computational grid consistently with the material motion. This similarity stems from the fact that the present approximate Riemann solver has an underlying Lagrangian structure, inherited from the Zha–Bilgen decomposition of the flux into convective and pressure contributions.

2.6 Domain-preserving CFL condition

The admissible set of physical states is the convex set

$$\mathcal{D} = \left\{ \mathbf{U} = (\rho, \rho\mathbf{v}, \rho e)^t \;\middle|\; \rho > 0 \text{ and } \rho e - \tfrac{1}{2}\rho|\mathbf{v}|^2 > 0 \right\}, \tag{19}$$

i.e., states with positive density and positive specific internal energy. The wave-speed computation described in the previous subsections ensures that all intermediate states of every Riemann problem lie in $\mathcal{D}$ whenever the left and right input states do: $\mathbf{U}_l, \mathbf{U}_r \in \mathcal{D} \implies \mathbf{U}_k \in \mathcal{D}$ for all $k \in [2, K]$. In general, for a simple approximate Riemann solver with K waves, the left-sided numerical flux decomposes over the waves as

$$\mathbf{F}^- = \mathbf{F}_l - \sum_{k=1}^{K} \Lambda_k^{(-)} \big(\mathbf{U}_{k+1} - \mathbf{U}_k\big), \tag{20}$$

where $x^{(-)} = (|x| - x)/2$, see [3]. Substituting (20) into the explicit Euler update

$$\mathbf{U}_c^{n+1} = \mathbf{U}_c^n - \frac{\Delta t}{|\omega_c|} \sum_{p \in \mathcal{P}(c)} \sum_{f \in \mathcal{SF}(pc)} A_{pcf} \, \mathbf{F}^n_{pcf} \tag{21}$$

and using the closed-cell identity $\sum_{p,f} A_{pcf} \, \mathbf{n}_{pcf} = \mathbf{0}$, one obtains the equivalent form

$$\mathbf{U}_c^{n+1} = \alpha_c \, \mathbf{U}_c^n + \sum_{p,f} \sum_{k=1}^{K-1} \alpha_{pcf,k} \, \mathbf{U}^n_{pcf,k+1} + \sum_{p,f} \alpha_{pcf,K} \, \mathbf{U}^n_d, \tag{22}$$

with weights

$$\begin{aligned}
\alpha_c &= 1 - \frac{\Delta t}{|\omega_c|} \sum_{p,f} A_{pcf}\, \Lambda^{(-)}_{pcf,1}, \\
\alpha_{pcf,k} &= \frac{\Delta t}{|\omega_c|} A_{pcf} \big(\Lambda^{(-)}_{pcf,k} - \Lambda^{(-)}_{pcf,k+1}\big) \geq 0 \quad \forall k \in [1, K-1], \\
\alpha_{pcf,K} &= \frac{\Delta t}{|\omega_c|} A_{pcf}\, \Lambda^{(-)}_{pcf,K} \geq 0.
\end{aligned} \tag{23}$$

The weights $\alpha_{pcf,k}$ are non-negative by the wave ordering $\Lambda^{(-)}_1 \geq \cdots \geq \Lambda^{(-)}_K$, and all weights sum to one. The weight α_c is non-negative under the CFL condition

$$\Delta t < \min_{c \in C} \frac{|\omega_c|}{\displaystyle\sum_{p \in \mathcal{P}(c)} \sum_{f \in \mathcal{SF}(pc)} A_{pcf}\, \Lambda^{(-)}_{pcf,1}}, \tag{24}$$

under which (22) is a genuine convex combination of states in $\mathcal{D}$, which therefore guarantees $\mathbf{U}^{n+1}_c \in \mathcal{D}$. This condition holds for all four schemes and guarantees positivity of density and internal energy at the next iteration.

2.7 First-order numerical results

2.7.1 Three-dimensional odd–even decoupling test

The odd–even decoupling test [10] is the standard benchmark for assessing sensitivity to mesh perturbations. The domain $[0, 800] \times [-10, 10] \times [-10, 10]$ is meshed with $800 \times 20 \times 20$ hexahedra. The center line of the mesh is perturbed by displacing the nodes in the yz-plane as

$$\tilde{\mathbf{x}}_p = \mathbf{x}_p + a_0\, (0,\, \cos\phi,\, \sin\phi)^t, \qquad \phi = \big(\mathbf{x}_p \cdot \mathbf{e}_x\big) \frac{\pi}{2}, \tag{25}$$

where a_0 is the perturbation amplitude. This produces a helical perturbation of the center line. A Mach-6 shock wave propagates in the $+\mathbf{e}_x$ direction; the exact solution is a perfectly planar shock. Three amplitudes $a_0 \in \{10^{-3},\ 10^{-6},\ 10^{-9}\}$ are tested.

Pressure isosurfaces at final time $t = 50$ are shown in Table 1. The three-wave scheme develops a pronounced carbuncle instability for all perturbation levels, regardless of how small the initial perturbation is. The two-wave, modified three-wave, and multi-point schemes all produce the correct planar shock without any visible perturbation. These results clearly demonstrate that the multidimensional coupling of the multi-point scheme and the tangential dissipation of the two-wave and modified three-wave schemes are effective carbuncle cures.

2.7.2 Sedov blast

The Sedov problem [12] is a point-blast in a uniform cold medium with spherical symmetry. The domain $[-1.2, 1.2]^3$ is meshed with three successive Cartesian grids of 64^3, 128^3, and 256^3 hexahedra. The initial conditions are

$$\big(\rho_0,\ \mathbf{v}_0,\ p_0\big) = \big(1,\ \mathbf{0},\ 10^{-6}\big), \quad \gamma = \tfrac{7}{5}, \tag{26}$$

with a total released energy $\mathcal{E}_0 = 0.851072$ [13]. The exact solution is a spherical diverging shock at radius $R = 1$ with peak density 6 at $t = 1$. This test case assesses the ability of a scheme to preserve the spherical symmetry of the solution on a non-conforming grid. On the 128^3 grid, the multi-point scheme better preserves spherical symmetry than all other schemes in scattered density plots (not shown), owing to the multidimensional character of its nodal velocity computation. On the finest grid (256^3), density isosurfaces are shown in Figure 4: the three-wave scheme develops visible carbuncle-type instabilities where the shock aligns with the grid axes, while the multi-point scheme remains stable and symmetric.

	Two-wave	Three-wave	Modified three-wave	Multi-point
$a_0 = 10^{-3}$		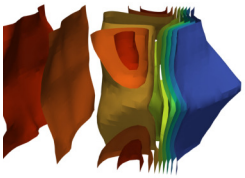		
$a_0 = 10^{-6}$		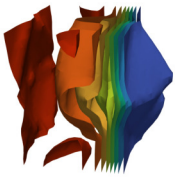		
$a_0 = 10^{-9}$				

Table 1: 3D odd–even decoupling: pressure isosurfaces at $t = 50$ for three perturbation amplitudes. The three-wave scheme is unstable for all amplitudes; the two-wave, modified three-wave, and multi-point schemes remain stable.

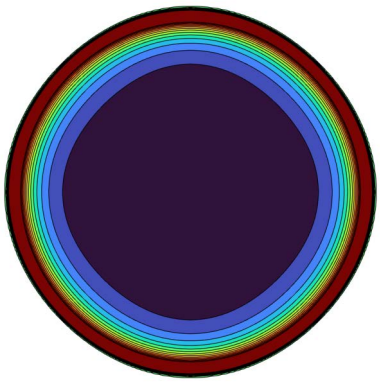

(a) Two-wave

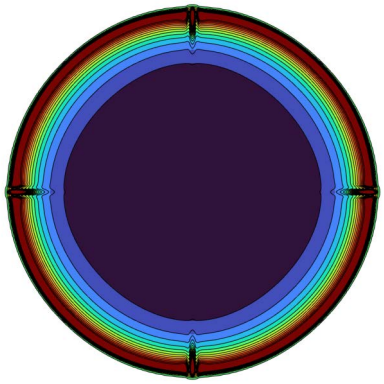

(b) Three-wave

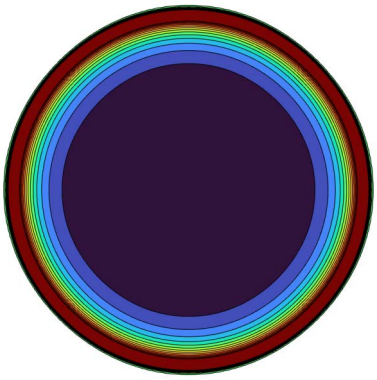

(c) Modified three-wave

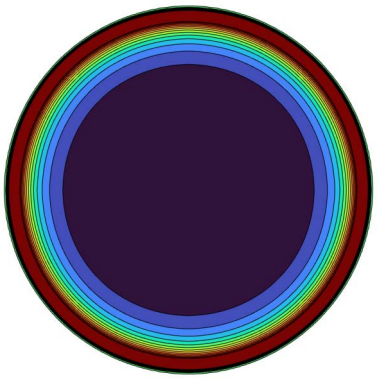

(d) Multi-point

Figure 4: Sedov blast on the 256^3 Cartesian grid: density isosurfaces at $t = 1$. Carbuncle instabilities appear in the three-wave scheme where the shock aligns with the grid axes.

2.7.3 Atmospheric Re-entry Demonstrator (ARD)

The flow conditions, identical to those in [14], are recalled in Table 2. The computational grid contains

Table 2: Freestream conditions for the ARD at Mach 24.

Mach [-]	24	Temperature [K]	224.5
Altitude [km]	65.83	Pressure [Pa]	10.23
Velocity [m/s]	7212.43	Wall temperature [K]	1500
Density [kg/m^3]	1.5869×10^{-4}	AoA [°]	20

4.8 million tetrahedra generated with Gmsh [15]. Figure 5 shows the pressure isosurfaces for the four schemes. The three-wave scheme develops a large carbuncle instability that completely corrupts the flow field. The two-wave, modified three-wave, and multi-point schemes all produce physically consistent bow shocks. Figure 6 compares the pressure coefficient $C_p = \frac{p_w - p_\infty}{\frac{1}{2}\rho_\infty |\mathbf{v}_\infty|^2}$ along the symmetry plane for all four schemes with flight measurements from [14].

3. Subface-based discretization of the heat conducting and viscous terms

The viscous and heat-conducting terms of the compressible Navier–Stokes equations are discretized within the same subface-based finite volume framework introduced in Section 2 for the inviscid part. The approach directly extends the scheme developed by Jacq [16] for three-dimensional anisotropic diffusion on unstructured polyhedral meshes, and the reader is referred to [5] for the complete derivation and validation.

3.1 Scalar problem: heat conduction

We can study the heat-conducting term in the energy equation by studying a simple heat conduction equation written in mixed form as

$$\rho C_v \frac{\partial \theta}{\partial t} + \nabla \cdot \mathbf{q} = 0, \qquad \mathbf{q} + \mathbb{K} \nabla \theta = \mathbf{0}, \tag{27}$$

where θ is the temperature, $\mathbf{q}$ the heat flux, and $\mathbb{K} = \kappa \mathbb{I}$ the isotropic conductivity tensor (with κ determined from the viscosity via a fixed Prandtl number $\mathrm{Pr} = 0.71$). The subface-based finite volume formulation of (27) writes

$$|\omega_c| \, \rho_c C_v \frac{\mathrm{d}\theta_c}{\mathrm{d}t} + \sum_{p \in \mathcal{P}(c)} \mathbf{q}_{pc} \cdot \mathbf{N}_{pc} = 0, \tag{28}$$

where $\mathbf{N}_{pc} = \sum_{f \in \mathcal{SF}(pc)} A_{pcf} \mathbf{n}_{pcf}$ is the outward area-weighted normal of subcell pc. The corner heat flux $\mathbf{q}_{pc}$ is approximated inside each subcell by assuming that the conductivity is uniform and equal to the cell-averaged value $\mathbb{K}_c$, and introducing an auxiliary subface temperature θ_{pf} on each subface

$$\mathbf{q}_{pc} = -\frac{\mathbb{K}_c}{|\omega_{pc}|} \sum_{f \in \mathcal{SF}(pc)} A_{pcf} (\theta_{pf} - \theta_c) \, \mathbf{n}_{pcf}. \tag{29}$$

The use of a single temperature θ_{pf} per subface automatically enforces temperature continuity across interfaces. The subface temperatures are then eliminated by requiring that the normal component of the heat flux be continuous across every subface. This condition is linear in the subface unknowns and yields, for each node p, a local linear system

$$\mathbb{M}_p \, \bar{\boldsymbol{\theta}}_p = \mathbb{S}_p \, \boldsymbol{\theta}_p, \tag{30}$$

where $\bar{\boldsymbol{\theta}}_p$ collects the subface temperatures around p and $\boldsymbol{\theta}_p$ the surrounding cell temperatures. Solving (30) at every node and back-substituting into (28) assembles a global sparse diffusion matrix that is

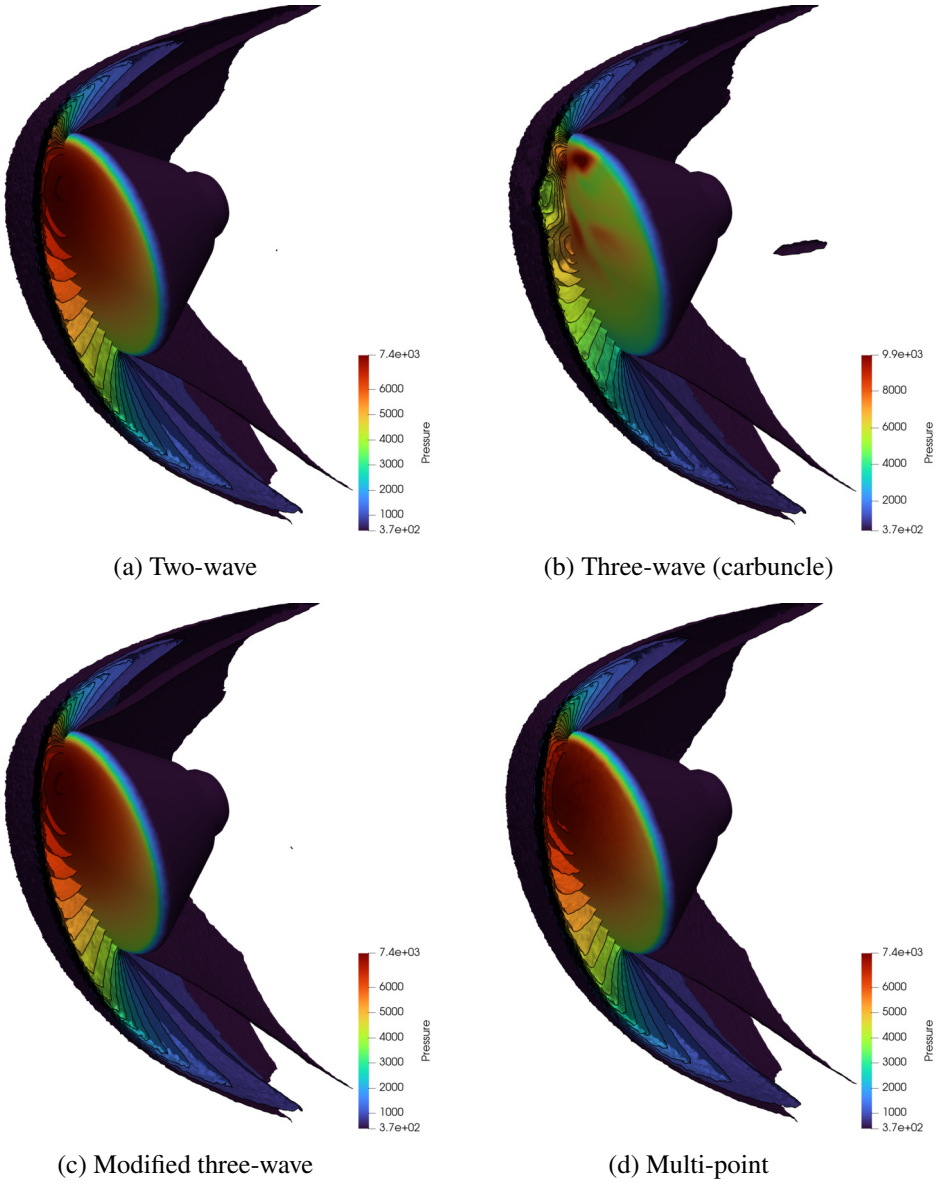

(a) Two-wave (b) Three-wave (carbuncle)

(c) Modified three-wave (d) Multi-point

Figure 5: ARD at Mach 24, 4.8M-tetrahedra grid: pressure isosurfaces for the four schemes. The three-wave scheme exhibits a carbuncle instability; the other three schemes produce clean bow shocks.

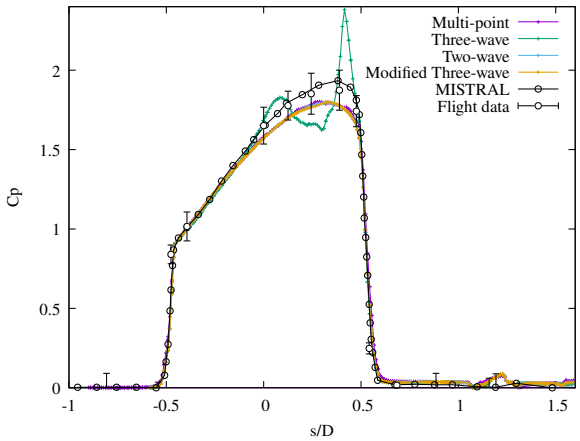

Figure 6: ARD at Mach 24: pressure coefficient C_p along the symmetry plane for the four Euler solvers. The multi-point scheme yields the best agreement with flight data from [14].

symmetric positive definite, a property inherited from the positive definiteness of $\mathbb{K}_c$. This scheme has been shown to be exact to capture linear fields on tetrahedra, regular hexahedra, and regular triangular basis prisms, and second-order accurate on arbitrary hexahedra, prisms, and pyramids, see [16, 17, 5]. This scheme allows us to discretize the divergence of the heat flux using the global diffusion matrix $\mathbb{D}^q$ and global vector of contribution from the boundary terms $\mathbf{B}^q$ as

$$\frac{1}{|\omega_c|}\int_{\omega_c} \nabla\cdot\mathbf{q}\,\mathrm{dv} = \sum_{d\in C(c)} [\mathbb{D}^q]_{c,d}\theta_d + [\mathbf{B}^q]_c. \tag{31}$$

3.2 Vectorial problem: viscous stress

We can study the discretization of the viscous terms by studying a vectorial diffusion equation of the form

$$\rho\frac{\partial \mathbf{v}}{\partial t} - \nabla\cdot\mathbb{S} = \mathbf{0}, \qquad \mathbb{S} = 2\mu\mathbb{D}_0, \tag{32}$$

where μ is the dynamic viscosity (computed via Sutherland's law), $\mathbb{D} = \frac{1}{2}[\nabla\mathbf{v} + (\nabla\mathbf{v})^t]$ is the strain-rate tensor, and $\mathbb{D}_0 = \mathbb{D} - \frac{1}{3}(\mathrm{tr}\,\mathbb{D})\mathbb{I}$ its deviatoric part. The discretization follows the same structure as the scalar case: a corner viscous stress tensor $\mathbb{S}_{pc}$ is approximated in each subcell using auxiliary subface velocities $\mathbf{v}_{pf}$, and the continuity of the normal stress across each subface produces a nodal linear system analogous to (30).

A key difficulty is that the constitutive law relating $\mathbb{S}$ to $\nabla\mathbf{v}$ is not invertible over the full space of second-order tensors (its kernel contains any antisymmetric tensor). Following the approach of [16] and inspired by [18], a divergence-free correction term is added to the constitutive law to make it invertible without altering the original governing equation. This correction and the detailed study of the scheme will be presented in a dedicated paper [19]. The resulting nodal system remains symmetric positive definite. The scheme has the same convergence properties as the scalar version, see [16, 17, 5].

Similarly to the scalar case, this scheme allows us to discretize the divergence of the viscous stress tensor using the global diffusion matrix (a block matrix with blocks of size $d\times d$), $\mathbb{D}^S$, and global vector of boundary contributions (a block vector with blocks of size d), $\mathbf{B}^S$, as

$$\frac{1}{|\omega_c|}\int_{\omega_c} -\nabla\cdot\mathbb{S}\,\mathrm{dv} = \sum_{d\in C(c)} [\mathbb{D}^S]_{c,d}\mathbf{v}_d + [\mathbf{B}^S]_c. \tag{33}$$

4. Three-dimensional Navier–Stokes equations

We describe here how the inviscid scheme of Section 2 is coupled with the diffusion scheme of Section 3 to solve the full compressible Navier–Stokes system. Following [16, 5], both the heat-conducting and viscous terms are treated *implicitly* in order to alleviate the quadratic time-step restriction that would arise from an explicit discretization of the diffusion operators on the highly anisotropic meshes encountered in viscous hypersonic computations. The Euler fluxes are initially treated explicitly, then incorporated into a point-implicit (PI) scheme [20] that preserves the domain-preserving property of the inviscid solver and makes the method equivalent to using a cell-local time step for the convective part.

4.1 Coupled formulation

The compressible Navier–Stokes equations can be written in the compact form

$$\frac{\partial \mathbf{U}}{\partial t} + \nabla\cdot\mathbb{F}^E(\mathbf{U}) = \nabla\cdot\mathbb{F}^S(\mathbf{U}) + \nabla\cdot\mathbb{F}^q(\mathbf{U}), \tag{34}$$

with $\mathbf{U} = (\rho,\ \rho\mathbf{v},\ \rho e)^t$, and where

$$\mathbb{F}^E = \mathbf{U} \otimes \mathbf{v} + \begin{pmatrix} \mathbf{0}^t \\ p\mathbb{I} \\ p\mathbf{v}^t \end{pmatrix}, \quad \mathbb{F}^S = \begin{pmatrix} \mathbf{0}^t \\ \mathbb{S} \\ (\mathbb{S}\mathbf{v})^t \end{pmatrix}, \quad \text{and} \quad \mathbb{F}^q = \begin{pmatrix} \mathbf{0}^t \\ \mathbb{0} \\ -\mathbf{q}^t \end{pmatrix}. \tag{35}$$

$\mathbb{F}^E$ gathers the inviscid (hyperbolic) fluxes, $\mathbb{F}^S$ the viscous stress tensor $\mathbb{S}$ and its power, and $\mathbb{F}^q$ the heat flux $\mathbf{q}$. The three contributions are discretized independently within the same subface framework and then assembled.

Contribution from the hyperbolic part. The inviscid contribution is handled with the subface-based multi-point scheme of Section 2

$$\int_{\omega_c} \nabla \cdot \mathbb{F}^E \,\mathrm{dv} = \sum_{p \in \mathcal{P}(c)} \sum_{f \in \mathcal{SF}(pc)} A_{pcf}\, \mathbf{F}_{pcf}, \tag{36}$$

where $\mathbf{F}_{pcf}$ is any of the multi-point Riemann solvers of Section 2.

Contribution from heat conduction. The scalar diffusion scheme of Section 3 produces a symmetric positive definite (SPD) diffusion matrix $\mathbb{D}^q$ acting on the cell temperatures θ_d

$$\int_{\omega_c} \nabla \cdot \mathbb{F}^q \,\mathrm{dv} = \begin{pmatrix} 0 \\ \mathbf{0} \\ -\sum_{d \in C(c)} [\mathbb{D}^q]_{c,d}\, \theta_d + [\mathbf{B}^q]_c \end{pmatrix}, \tag{37}$$

where $\mathbf{B}^q$ contains the thermal boundary contributions.

Contribution from viscous stress. The vectorial diffusion scheme of Section 3 similarly produces an SPD matrix $\mathbb{D}^S$ acting on cell velocities $\mathbf{v}_d$. In the energy equation, the power of the viscous forces involves the product $\mathbb{S}\mathbf{v}$ and is computed explicitly from the corner stress tensors $\mathbb{S}_{pc}$ and the subface velocities $\bar{\mathbf{v}}_{pcf}$ already available from the nodal solve of the diffusion system

$$\int_{\omega_c} \nabla \cdot \mathbb{F}^S \,\mathrm{dv} = \begin{pmatrix} \mathbf{0} \\ -\sum_{d \in C(c)} [\mathbb{D}^S]_{c,d}\, \mathbf{v}_d + [\mathbf{B}^S]_c \\ \sum_{p \in \mathcal{P}(c)} \sum_{f \in \mathcal{SF}(pc)} A_{pcf}\, \mathbb{S}_{pc}\big(\bar{\mathbf{v}}_{pcf} - \mathbf{v}_c\big) \cdot \mathbf{n}_{pcf} \end{pmatrix}. \tag{38}$$

Semi-discrete scheme. Gathering equations (36), (38), and (37) gives the full semi-discrete Navier–Stokes scheme for each cell ω_c

$$|\omega_c| \frac{\mathrm{d}\mathbf{U}_c}{\mathrm{d}t} + \sum_{p \in \mathcal{P}(c)} \sum_{f \in \mathcal{SF}(pc)} A_{pcf}\, \mathbf{F}_{pcf} = \begin{pmatrix} 0 \\ -\sum_{d \in C(c)} [\mathbb{D}^S]_{c,d} \mathbf{v}_d + [\mathbf{B}^S]_c \\ \sum_{p \in \mathcal{P}(c)} \sum_{f \in \mathcal{SF}(pc)} A_{pcf} \mathbb{S}_{pc}(\bar{\mathbf{v}}_{pcf} - \mathbf{v}_c) \cdot \mathbf{n}_{pcf} - \sum_{d \in C(c)} [\mathbb{D}^q]_{c,d} \theta_d + [\mathbf{B}^q]_c \end{pmatrix}. \tag{39}$$

Both flux contributions share the same subface geometry and assembly structure, making the implementation straightforward. The stencil of each cell involves only its node-connected neighbors $C(c) = \cup_{p \in \mathcal{P}(c)} C(p)$, which limits fill-in and facilitates parallel computation.

4.2 Implicit treatment and global linear system

In Navier–Stokes computations the mesh is strongly anisotropic near solid walls in order to resolve the boundary layer. On such meshes an explicit time step for the diffusion operators would be proportional to $h_\perp^2/\nu$ where $h_\perp$ is the wall-normal cell size, leading to prohibitively small time steps. We therefore discretize the heat-conducting and viscous terms at time level $n+1$ while keeping the Euler fluxes at the known level n

$$\frac{|\omega_c|}{\Delta t}\left(\mathbf{U}_c^{n+1}-\mathbf{U}_c^{n}\right)+\begin{pmatrix}0\\ \displaystyle\sum_{d\in\mathcal{C}(c)}[\mathbb{D}^S]_{c,d}\mathbf{v}_d^{n+1}\\ \displaystyle\sum_{d\in\mathcal{C}(c)}[\mathbb{D}^q]_{c,d}\theta_d^{n+1}\end{pmatrix}=-\sum_{p\in\mathcal{P}(c)}\sum_{f\in\mathcal{SF}(pc)}A_{pcf}\,\mathbf{F}_{pcf}^{n}+\begin{pmatrix}0\\ [\mathbf{B}^{S,n}]_c\\ \displaystyle\sum_{p,f}A_{pcf}\mathbb{S}_{pc}(\bar{\mathbf{v}}_{pcf}^{n}-\mathbf{v}_c^{n})\cdot\mathbf{n}_{pcf}+[\mathbf{B}^{q,n}]_c\end{pmatrix}. \tag{40}$$

The matrices $\mathbb{D}^S$ and $\mathbb{D}^q$ operate respectively on velocity $\mathbf{v}$ and temperature θ, but the global system must be assembled in conservative variables $\mathbf{U}$. This requires introducing first-order linearizations of the primitive variables at time $n+1$ in terms of $\Delta\mathbf{U}=\mathbf{U}^{n+1}-\mathbf{U}^n$

$$\mathbf{v}^{n+1}\approx\mathbf{v}^n+\left(\frac{\mathrm{d}\mathbf{v}}{\mathrm{d}\mathbf{U}}\right)^n\Delta\mathbf{U},\qquad \theta^{n+1}\approx\theta^n+\left(\frac{\mathrm{d}\theta}{\mathrm{d}\mathbf{U}}\right)^n\Delta\mathbf{U}, \tag{41}$$

where the change-of-variable Jacobians are

$$\frac{\mathrm{d}\mathbf{v}}{\mathrm{d}\mathbf{U}}=\left(-\frac{\mathbf{v}}{\rho},\ \frac{1}{\rho}\mathbb{I},\ \mathbf{0}\right),\qquad \frac{\mathrm{d}\theta}{\mathrm{d}\mathbf{U}}=\frac{1}{\rho C_v}\left(-(e+|\mathbf{v}|^2),\ -\mathbf{v}^t,\ 1\right). \tag{42}$$

Defining modified matrices $\tilde{\mathbb{D}}^S$ and $\tilde{\mathbb{D}}^q$ that embed the Jacobians (42),

$$[\tilde{\mathbb{D}}^S]_{c,d}=\begin{pmatrix}\mathbf{0}^t\\ [\mathbb{D}^S]_{c,d}\left(\dfrac{\mathrm{d}\mathbf{v}}{\mathrm{d}\mathbf{U}}\right)_c\\ \mathbf{0}^t\end{pmatrix},\qquad [\tilde{\mathbb{D}}^q]_{c,d}=\begin{pmatrix}\mathbf{0}^t\\ \mathbb{0}\\ [\mathbb{D}^q]_{c,d}\left(\dfrac{\mathrm{d}\theta}{\mathrm{d}\mathbf{U}}\right)_c\end{pmatrix}, \tag{43}$$

the system (40) can be rewritten as a single global linear system in conservative variable increments

$$\mathbb{M}^n\,\Delta\mathbf{U}=\mathbf{R}^n, \tag{44}$$

with block structure

$$[\mathbb{M}]_{c,d}=\frac{|\omega_c|}{\Delta t}\,\mathbb{I}\,\delta_{cd}+[\tilde{\mathbb{D}}^S]_{c,d}+[\tilde{\mathbb{D}}^q]_{c,d}, \tag{45}$$

and right-hand side

$$[\mathbf{R}]_c^n=-\sum_{p,f}A_{pcf}\,\mathbf{F}_{pcf}^n+\begin{pmatrix}0\\ -\displaystyle\sum_d[\mathbb{D}^S]_{c,d}\mathbf{v}_c^n-[\mathbf{B}^{S,n}]_c\\ -\displaystyle\sum_d[\mathbb{D}^q]_{c,d}\theta_c^n-[\mathbf{B}^{q,n}]_c+\sum_{p,f}A_{pcf}\mathbb{S}_{pc}(\bar{\mathbf{v}}_{pcf}^n-\mathbf{v}_c^n)\cdot\mathbf{n}_{pcf}\end{pmatrix}. \tag{46}$$

However, because storing the matrix $\mathbb{M}$ explicitly is not practical, we use a matrix-free strategy coupled with a point implicit treatment of the Eulerian fluxes explained in the next section.

4.3 Numerical results: supersonic flow over an adiabatic plate

We validate the coupled NS scheme on the supersonic flow over an adiabatic flat plate introduced in [21]. The plate extends from $x = 0$ to $x = 1$; the computational domain is $\Omega = [-0.1, 1] \times [0, 0.2] \times [0, 0.1]$. A geometric cell-size progression is imposed from both the leading edge ($x = 0$) and the wall ($y = 0$), with 10 cells for $x \in [-0.1, 0]$ (ratio 1.25), 40 cells for $x \in [0, 1]$ (ratio 1.12), and 30 cells for $y \in [0, 0.2]$ (ratio 1.15). The domain is a single layer in the z direction. The free-stream and fluid parameters are summarized in Table 3.

Table 3: Parameters for the supersonic flow over an adiabatic plate [21].

M_∞	1.7605	Re_{unit} (m^{-1})	2.88×10^5
ρ_∞ (kg m^{-3})	10^{-3}	Pr	0.71
$\mathbf{V}_\infty$ (m s^{-1})	500	μ (Pa s)	1.737×10^{-5}
p_∞ (Pa)	57.62	κ ($\text{W m}^{-1}\text{K}^{-1}$)	2.644×10^{-2}
θ_∞ (K)	300	wall	adiabatic

Figure 7 compares the velocity profiles in the wall-normal direction at $x = 0.5$ obtained with the three-wave, modified three-wave, two-wave, and multi-point schemes, both at first order (left) and second order (right). At first order, two categories of schemes can clearly be identified. The three-wave and multi-point

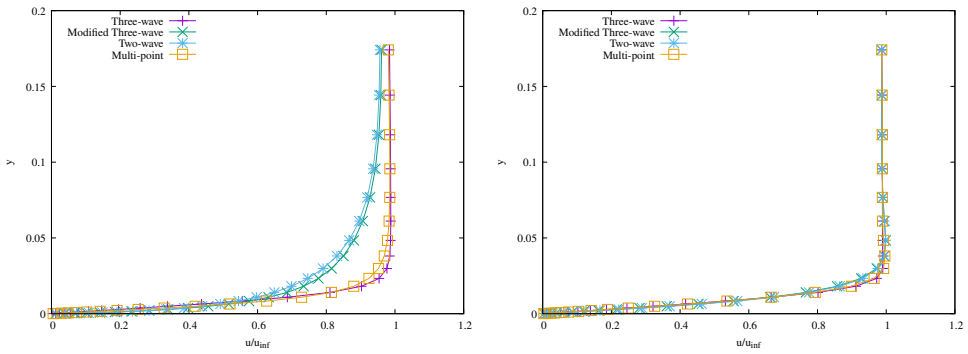

(a) First order (b) Second order

Figure 7: Velocity in the x direction as a function of the wall-normal distance at $x = 0.5$ computed with the various schemes.

schemes produce velocity profiles that are very close to each other, while the two-wave and modified three-wave schemes produce noticeably more diffused profiles. This difference is expected: the two-wave and modified three-wave solvers introduce explicit numerical diffusion of the tangential velocity in the intermediate region of the Riemann problem, which contaminates the boundary layer resolution at first order. The multi-point scheme, although also based on a nodal velocity average, diffuses shear layers in a fundamentally different way that is much less detrimental for boundary layer flows. At second order, the excessive diffusion introduced by the two-wave and modified three-wave schemes is corrected to the point that all four schemes produce almost identical velocity and temperature profiles. These results highlight the benefit of the second-order extension, which removes the first-order scheme-dependent error in the boundary layer and leads to an accurate resolution of the viscous flow regardless of the choice of Riemann solver. In the next section, we study in more detail the specific way the various schemes resolve a shear line with respect to its alignment to the mesh and the aspect ratio of the elements.

4.4 Numerical evaluation of the diffusion of the Eulerian schemes

A critical characteristic of numerical schemes for the Euler equations is their ability to resolve shear lines correctly. This is especially important when these schemes are used to solve the Navier–Stokes system,

where the numerical viscosity competes with the physical viscosity in boundary layer flows and may lead to incorrect heat-flux evaluation. It is therefore desirable to know a priori whether a given inviscid scheme will produce accurate heat fluxes when coupled with the diffusion discretization. The classical indicator is whether a scheme resolves exactly a shear line that is aligned with the mesh. If it does (as the three-wave scheme), the scheme is expected to produce accurate heat fluxes; if it does not, numerical diffusion of the tangential velocity contaminates the boundary layer. This question is however more subtle than it appears: the accuracy depends not only on the scheme but also on the orientation of the shear line with respect to the mesh and on the element aspect ratio as we shall see. In this section we propose a systematic study by rotating the shear line and varying the anisotropy of the mesh, a more thorough study as well as the by hand computation of the error for the different schemes can be found in [5].

4.4.1 Description of the test

The test consists in initializing two constant states $\mathbf{W}_l$ and $\mathbf{W}_r$ on either side of a discontinuity. The domain is $\Omega = [-1, 1]^2$; the discontinuity passes through the origin at angle θ from the horizontal x axis. The primitive states are

$$\mathbf{W}_l = (1, V_l\,\mathbf{e}_R, 1)^t, \qquad \mathbf{W}_r = (1, V_r\,\mathbf{e}_R, 1)^t, \tag{47}$$

where $\mathbf{e}_R = (\cos\theta, \sin\theta, 0)^t$ and $V_l = 1$, $V_r = -1$. A Cartesian mesh is used so that the shear line is aligned with the grid when $\theta = 0$ or $\theta = 90°$. Only one iteration of the scheme is performed: the explicit update ensures that boundary disturbances travel at most one cell layer, so the error can be evaluated on the interior of the domain without influence from the boundaries. The $\mathcal{L}^1$ error on the velocity field is computed for angles in $[0°, 360°]$ with steps of $5°$.

4.4.2 Numerical results

Figure 8 shows the solution after one iteration with the three-wave scheme for four orientations of the shear line on a 10×10 mesh, and Figure 9 shows the corresponding results on a 40×10 mesh to illustrate the effect of aspect ratio. Figure 10 shows the $\mathcal{L}^1$ error on the velocity as a function of the shear line

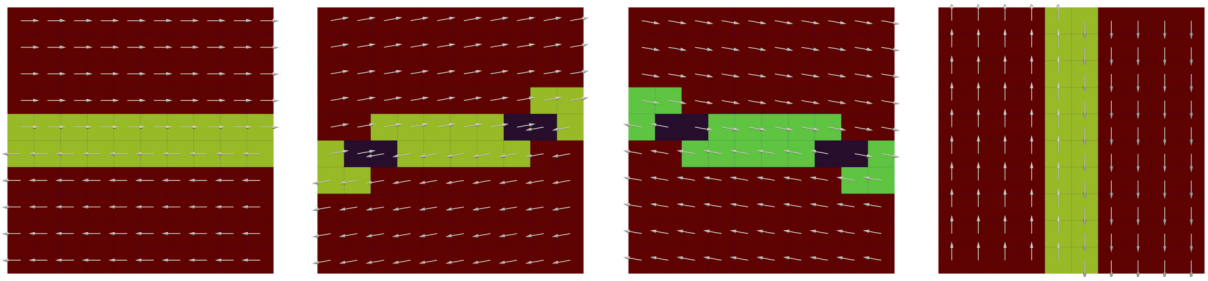

(a) $\theta = 0$ (b) $\theta = 10°$ (c) $\theta = -10°$ (d) $\theta = 90°$

Figure 8: Solution after one iteration with the three-wave scheme on a 10×10 mesh for four orientations of the shear line.

angle on Cartesian meshes of increasing anisotropy. The three-wave scheme resolves exactly shear lines aligned with the mesh ($\theta = 0, 90, 180, 270°$) whereas all the other schemes introduce some error. On the isotropic mesh (a), the schemes behave somewhat similarly, however, as the aspect ratio increases from 1 (a) to 4 (b), the multi-point scheme diverges significantly from the two-wave and modified three-wave schemes: it diffuses much **more** at $\theta = 0°$ (shear line along the refined x direction) but much **less** at $\theta = 90°$ (shear line perpendicular to the wall-normal refined direction). The latter configuration is exactly the one encountered in boundary layer meshes, which explains the superior performance of the multi-point scheme observed in Section 4.3.

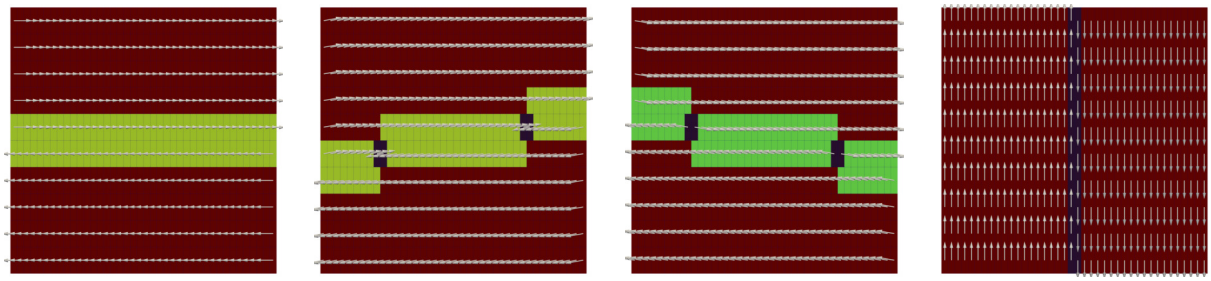

(a) $\theta = 0$ (b) $\theta = 10°$ (c) $\theta = -10°$ (d) $\theta = 90°$

Figure 9: Solution after one iteration with the three-wave scheme on a 40×10 mesh for four orientations of the shear line.

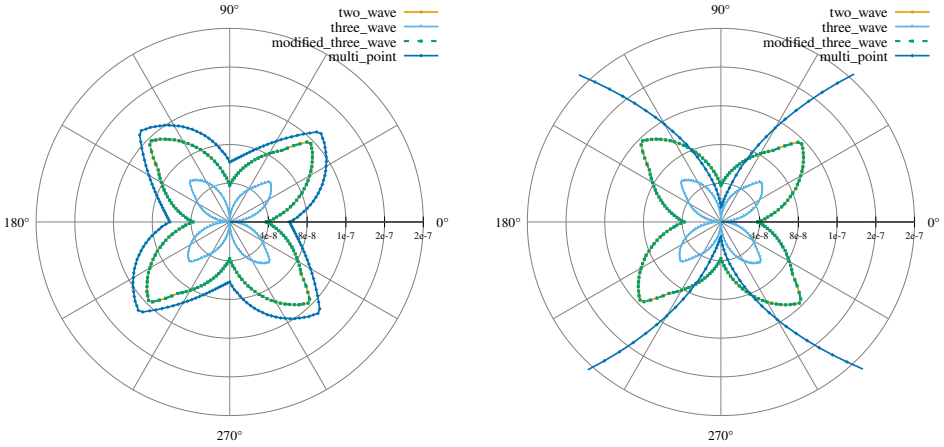

(a) 200×200 cells (b) 800×200 cells

Figure 10: Radial plots of the $\mathcal{L}^1$ velocity error as a function of the shear line angle for meshes of increasing anisotropy. At $\theta = 0°$ the shear line is aligned with the x axis.

4.4.3 Isotropic multi-point scheme

While the multi-point scheme is accurate for shear lines that are normal to the refined direction, its error grows proportionally to the aspect ratio when the mesh is refined along the shear line. To remedy this, we adopt a *composite* formulation [22, 23, 24, 25] in which each subface flux is a convex combination of the multi-point flux evaluated at the nodal velocity $\mathbf{v}_p$ and the same multi-point flux evaluated at the Godunov velocity $\bar{v}_{pcf}$

$$\int_{\omega_c} \nabla \cdot \mathbb{F}^E \, \mathrm{dv} = \sum_{p \in \mathcal{P}(c)} \sum_{f \in \mathcal{SF}(pc)} A_{pcf} \Big[\omega_{pf} \, \mathbf{F}_{pcf}(\mathbf{U}_c, \mathbf{U}_d, \mathbf{v}_p \cdot \mathbf{n}_{pcf}) + (1 - \omega_{pf}) \, \mathbf{F}_{pcf}(\mathbf{U}_c, \mathbf{U}_d, \bar{v}_{pcf}) \Big], \quad (48)$$

where d is the cell neighboring c across subface pcf and $\omega_{pf} \in [0, 1]$ is a face-based weight. This can be interpreted as a quadrature of the boundary integral where ω_{pf} weights a nodal quadrature point at p against a face-based point. Note that the multi-point flux fed with the Godunov velocity $\bar{v}_{pcf}$ degenerates to the classical three-wave flux, so this formulation recovers the three-wave scheme in the limit $\omega_{pf} \to 0$. The *isotropic* multi-point scheme [5] is then obtained by choosing ω_{pf} to cancel the area anisotropy in

the nodal system

$$\omega_{pf} = \frac{\min\limits_{g \in \mathcal{SF}(p)} A_{pg}}{A_{pf}}. \tag{49}$$

The nodal system then becomes

$$\left[\sum_{f \in \mathcal{SF}(p)} (\lambda_{pf,l} + \lambda_{pf,r})\, \mathbf{n}_{pf} \otimes \mathbf{n}_{pf} \right] \mathbf{v}_p = \sum_{f \in \mathcal{SF}(p)} (\lambda_{pf,l} + \lambda_{pf,r})\, \bar{v}_{pf}\, \mathbf{n}_{pf}, \tag{50}$$

which no longer depends on the face areas. This scheme preserves the favorable property of the multi-point scheme (error decreases with normal-direction refinement) while preventing the error from growing when the mesh is refined along the shear line. The corresponding radial plots are shown in Figure 11, where the isotropic multi-point scheme clearly maintains the same favorable scaling as the classical multi-point scheme for refinement in the normal direction of the shear line but no longer exhibits the anomalous growth with the refinement along the shear direction.

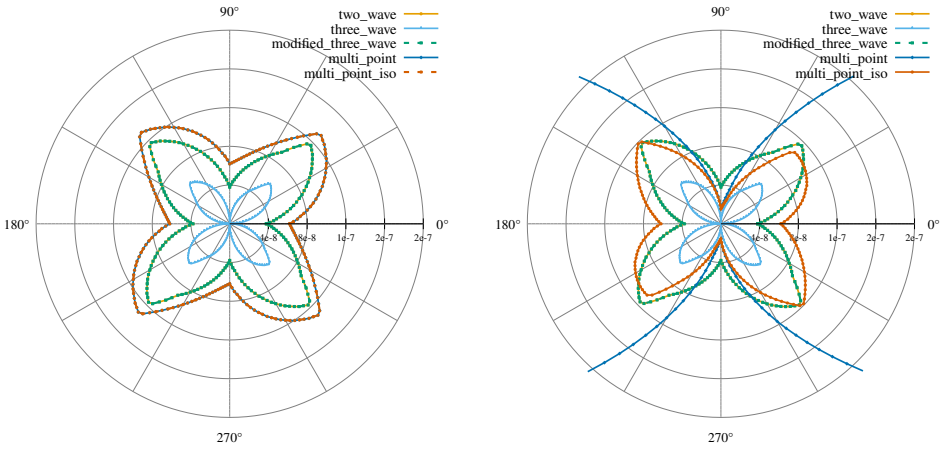

(a) 200×200 cells (b) 800×200 cells

Figure 11: Radial plots of the $\mathcal{L}^1$ velocity error including the isotropic multi-point scheme, for meshes of increasing anisotropy.

4.5 Numerical results: half-cylinder at Mach 17.605

In this section, we study a cylinder at Mach 17.605 taken from [26]. Adherence wall boundary conditions are applied on the surface of the cylinder with an imposed wall temperature $\theta_{\text{wall}} = 500$ K. Table 4 recalls the flow parameters. Two mesh types are studied: the aligned quadrangular (hexahedral) mesh presented in Figure 12, with 128 cells in the tangential direction and 64 cells in the normal direction, and the hybrid quad/tri mesh of Figure 14, with 156 tangential cells and 24 radial cells in the boundary layer. Results are obtained for three wall-normal refinement levels corresponding to a first-cell size $d_{\text{wall}} \in \{10^{-2}, 10^{-3}, 10^{-4}\}$.

Table 4: Parameters for the half-cylinder at Mach 17.605.

γ	1.4	μ	Dynamic, Sutherland's law
C_p (J·kg^{-1}·K^{-1})	1005.4719	κ	Dynamic, Prandtl number
C_v (J·kg^{-1}·K^{-1})	718.1942	θ_∞ (K)	200
ρ_∞ (kg·m^{-3})	10^{-3}	θ_{wall} (K)	500
$\mathbf{V}_\infty$ (m·s^{-1})	5000	Ma_∞	17.605
p_∞ (Pa)	57.6155768	Pr	0.71
μ_∞ (Pa·s)	3.2811×10^{-6}	Re_L (m^{-1})	3.7693×10^5

4.5.1 Hexahedral mesh

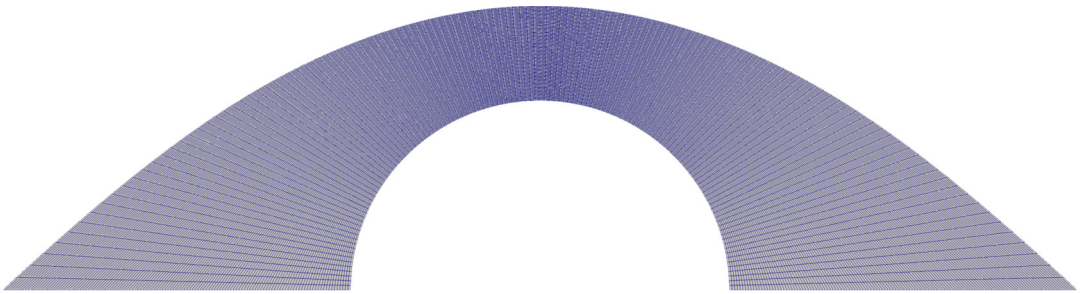

Figure 12: Hexahedral mesh used for computations on the half-cylinder at Mach 17.605 with wall cell size $d_{\text{wall}} = 10^{-2}$. There are 128 cells in the tangential direction and 64 cells in the normal direction.

For the temperature, the two-wave scheme produces a boundary layer far wider than the other schemes at first order. The three-wave scheme yields an incorrect solution even at first order. The modified three-wave and multi-point schemes look similar at first order, with the second-order extension strongly reducing diffusion near the wall. Figure 13 shows the Stanton number quantitatively: at first order the two-wave scheme is roughly one order of magnitude off in heat flux due to excessive diffusion. The first-order modified three-wave scheme does not converge to the correct heat flux even on the finest mesh, consistent with the analysis of Section 4.4. Both the multi-point and isotropic multi-point schemes correctly capture the heat flux at first order on the finest mesh.

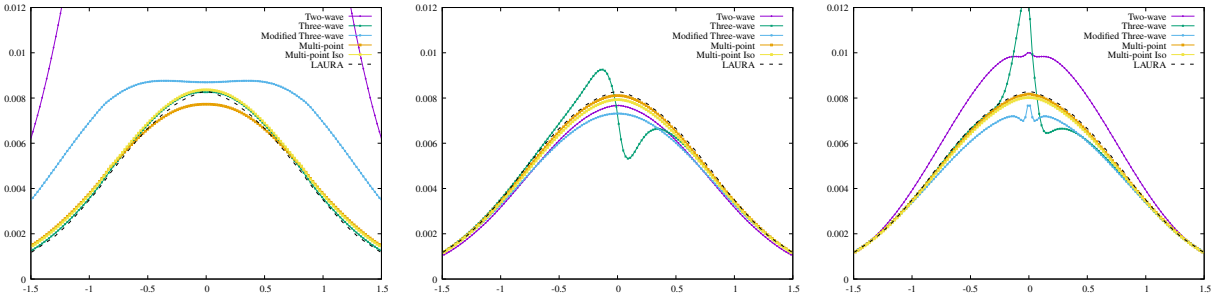

(a) First order (b) 2nd-order M2 (c) 2nd-order M4

Figure 13: Stanton number as a function of the angle for the half-cylinder at Mach 17.605 with a **hexahedral** mesh, finest boundary refinement ($d_{\text{wall}} = 10^{-4}$).

4.5.2 Hybrid quad/tri mesh

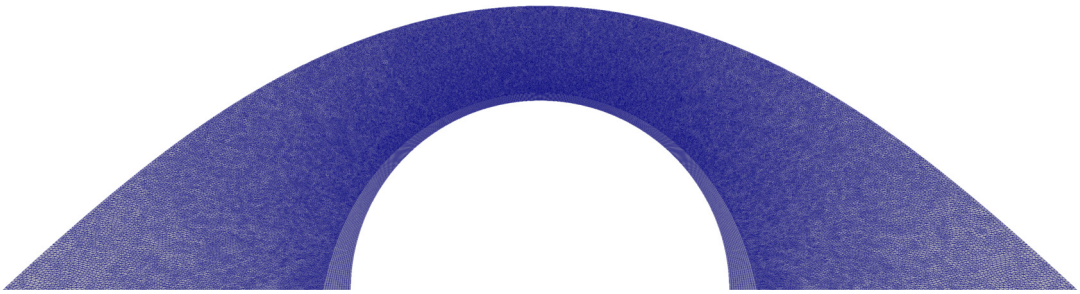

Figure 14: Hybrid quad/tri mesh used for computations on the half-cylinder at Mach 17.605 with wall cell size $d_{\text{wall}} = 10^{-2}$. There are 156 cells in the tangential direction and 24 cells in the radial direction in the boundary layer, with prisms in the far field.

The Stanton number plots in Figure 15 confirm the same behavior as on the hexahedral mesh: the modified three-wave scheme fails to converge to the correct heat flux with normal-direction refinement, while the multi-point and isotropic multi-point schemes achieve accurate heat flux prediction already at first order on the finest mesh, with further improvement at second order. We emphasize that results on the hybrid triangular mesh are particularly sensitive to the reconstruction strategy and limiting procedure employed.

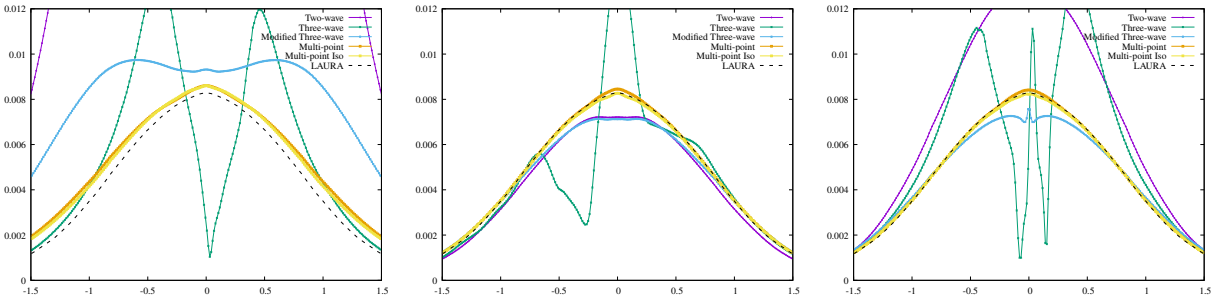

(a) First order (b) 2nd-order M2 (c) 2nd-order M4

Figure 15: Stanton number as a function of the angle for the half-cylinder at Mach 17.605 with a **hybrid quad/tri** mesh, finest boundary refinement ($d_{\text{wall}} = 10^{-4}$).

4.6 Atmospheric Re-entry Demonstrator at Mach 24

In this section, we study the impact of the mesh type on the heat flux computation for the Mach 24 flow around the Atmospheric Re-entry Demonstrator (ARD) already described in Section 2.7.3. Results are obtained at first order only, with emphasis on the differences between mesh types. Numerical results are compared to the block-structured reference code MISTRAL from R. Tech [27].

4.6.1 Block-structured hexahedral mesh

The first mesh is a block-structured mesh aligned with the shock (see Figure 16), generated with GridPro from a shock surface extracted from a coarse tetrahedral mesh, courtesy of Martin Spel from R. Tech. Two refinement levels are used: a coarse mesh with 120 000 hexahedral cells and a medium mesh with 960 000 cells (obtained by cutting each hexahedron into eight). Three first-cell sizes are tested: 10^{-4}, 10^{-5}, and 10^{-6}. The nomenclature is given in Table 5.

Table 5: Nomenclature for the ARD block-structured meshes.

		First cell size		
		10^{-4}	10^{-5}	10^{-6}
Number of elements	120 000	NS4C	NS5C	NS6C
	960 000	NS4M	NS5M	NS6M

The heat fluxes computed with the various Eulerian schemes on the NS4C mesh are presented in Figure 17. Because the ARD is at an angle of attack of 20°, a boundary-layer thinning phenomenon occurs on the ledge of the heat shield causing a sharp increase in temperature. The peak temperature reported in [14] is around 10^6 K, which is used as the maximum scale in Figure 17. The two-wave scheme produces a temperature on the heat shield far above the reported maximum. The three-wave scheme produces instabilities starting at the shock that propagate to the boundary layer and lead to erratic heat flux prediction. The modified three-wave scheme predicts the sharp increase on the edge but keeps the temperature too high over the full heat shield (instead of remaining close to 4×10^5 K). Both the multi-point and isotropic multi-point schemes correctly predict the sharp increase on the edge and the lower temperature on the remainder of the surface. The heat flux along the symmetry plane is shown in Figure 18. The multi-point scheme shows an anomalous sharp decrease right behind the leading edge, attributed to excessive longitudinal diffusion on anisotropic meshes (Section 4.4), while the isotropic version produces a result very close to the MISTRAL reference. Figure 18 (b) confirms that the isotropic multi-point scheme gives robust, accurate heat flux prediction across all mesh variants (NS4C, NS5C, NS6C, NS4M, NS5M, NS6M).

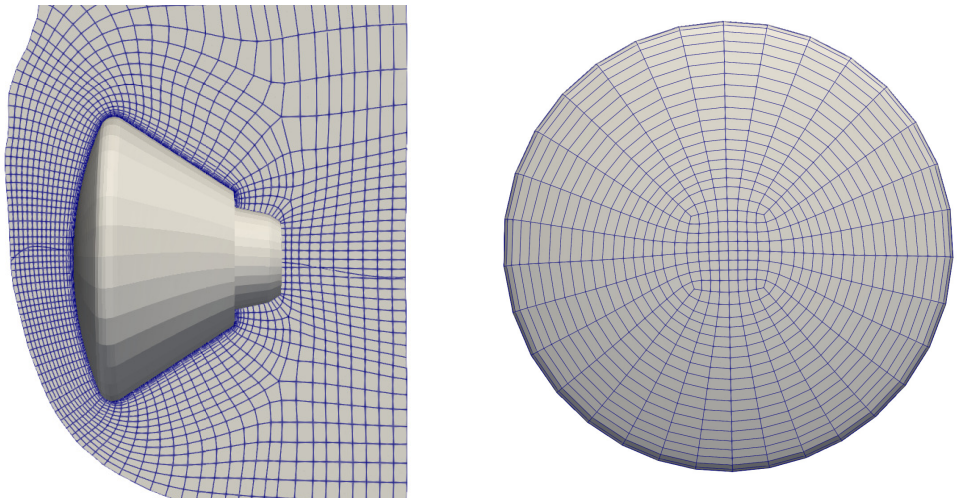

Figure 16: Aligned block-structured hexahedral mesh around the ARD generated with GridPro (NS4C mesh).

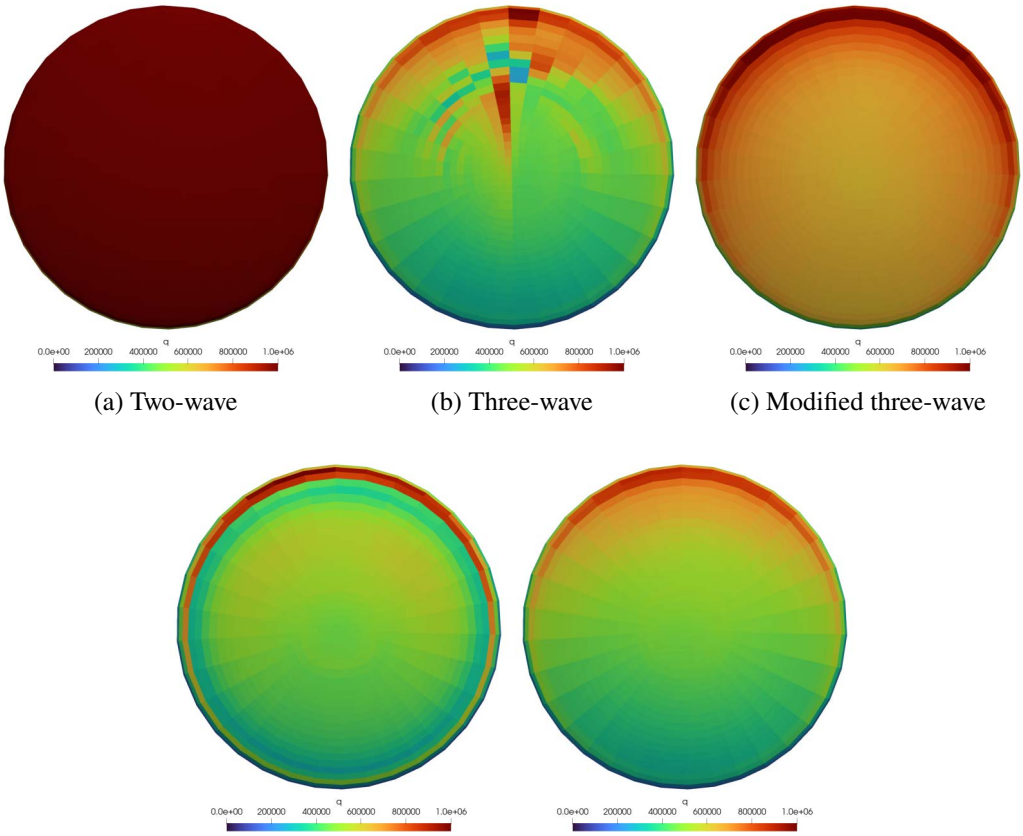

(a) Two-wave (b) Three-wave (c) Modified three-wave

(d) Multi-point (e) Isotropic multi-point

Figure 17: Heat flux on the surface of the ARD at Mach 24, NS4C mesh, all five Eulerian schemes.

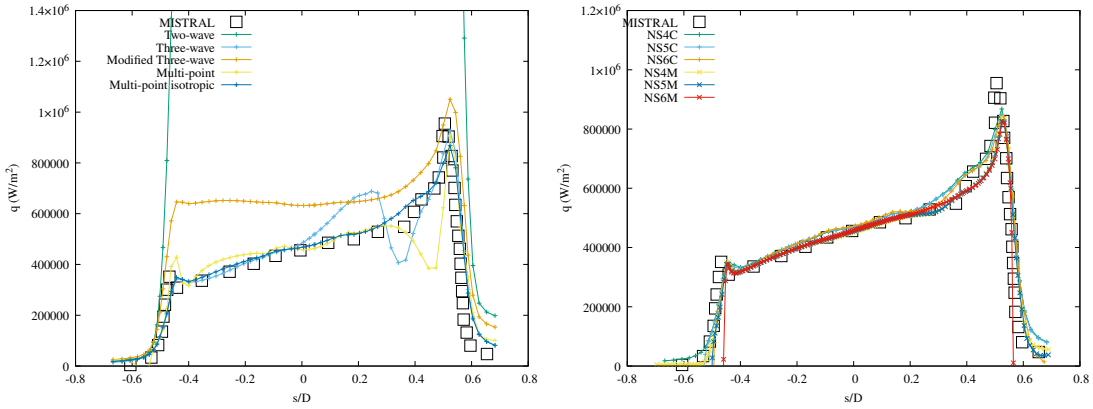

(a) Scheme comparison (NS4C) (b) Isotropic multi-point, all meshes

Figure 18: Heat flux along the symmetry plane of the ARD at Mach 24 on the block-structured mesh: (a) all schemes on NS4C, (b) isotropic multi-point scheme on the full set of meshes.

4.6.2 Hybrid tetrahedral mesh

The last mesh consists of tetrahedra in the far field and a prismatic boundary layer (Figure 19). This is a challenging configuration because the strong shock propagates through coarse tetrahedra, generating perturbations analogous to those observed on the hybrid cylinder mesh. The three-wave scheme shows clear shock perturbations that propagate into the boundary layer, yielding an erratic heat flux (Figure 20). The two-wave scheme overestimates the heat flux. The modified three-wave scheme still predicts a heat

flux that is too high near the low-temperature edge. In a striking result, the isotropic multi-point scheme produces a heat flux along the symmetry plane that is almost exactly on the MISTRAL reference solution (Figure 21), despite the coarseness of the tetrahedral region, with only some residual marbling of the surface heat flux visible in Figure 20.

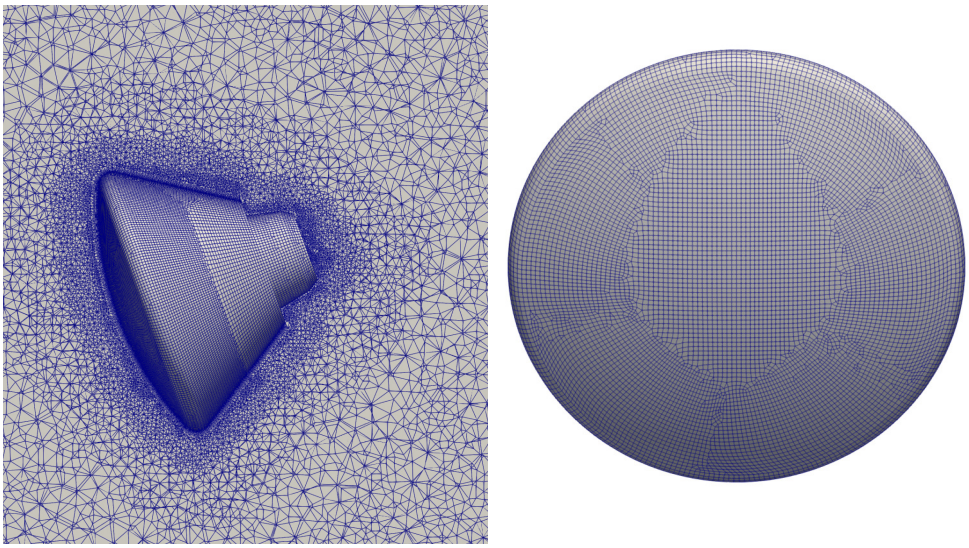

(a) (b)

Figure 19: Hybrid tetrahedral mesh around the ARD (tetrahedra in the far field, prismatic boundary layer).

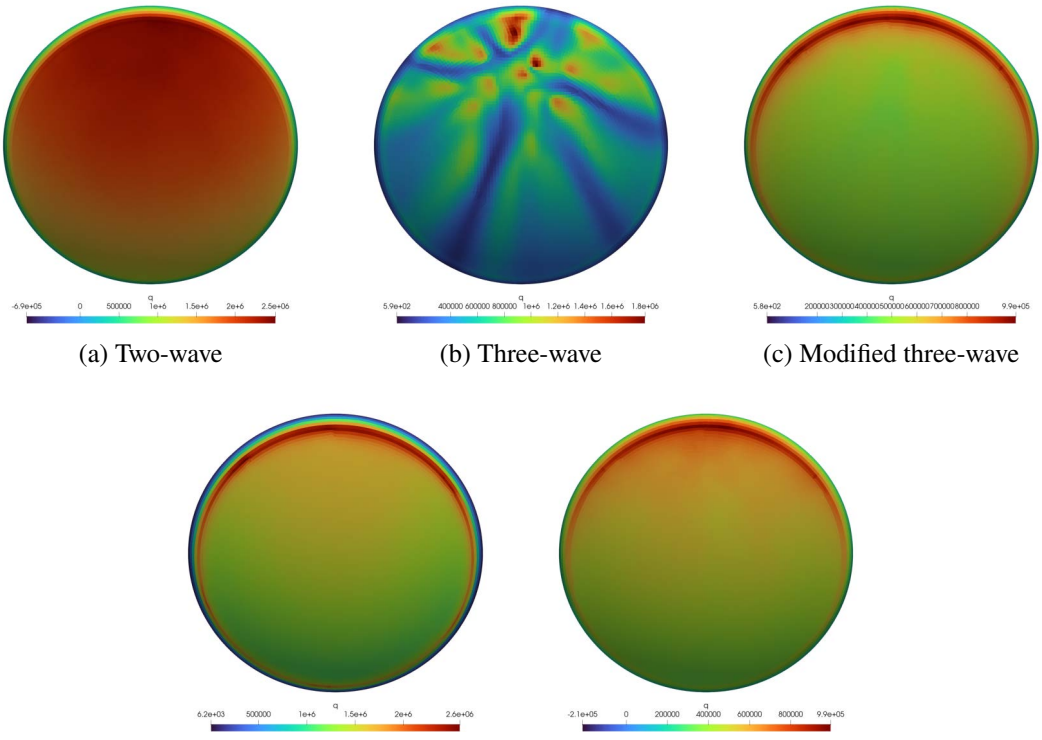

(a) Two-wave (b) Three-wave (c) Modified three-wave

(d) Multi-point (e) Isotropic multi-point

Figure 20: Heat flux on the surface of the ARD, hybrid tetrahedral mesh.

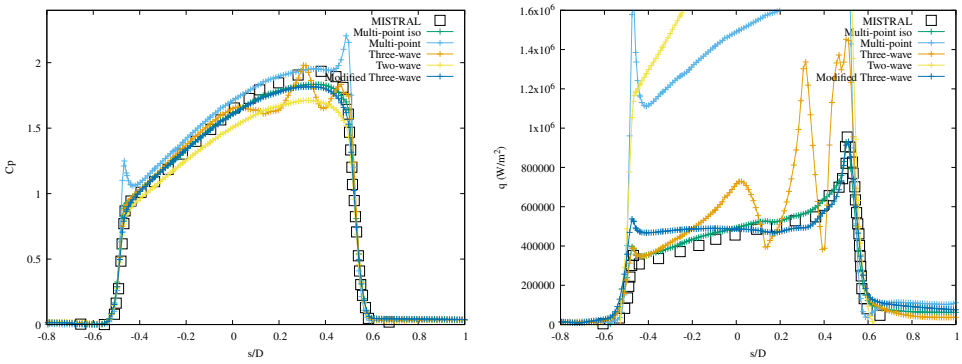

(a) (b)

Figure 21: Pressure coefficient (a) and heat flux (b) along the symmetry plane of the ARD on the hybrid tetrahedral mesh.

5. Conclusion

This paper has presented several contributions toward the development of robust and accurate numerical methods for hypersonic flows on unstructured hybrid grids.

A node-conservative, domain-preserving Euler scheme was derived within a subface-based finite volume framework. The multi-point Riemann solver couples all Riemann problems around each mesh node through a common nodal velocity, providing a genuinely multidimensional upwind flux that eliminates carbuncle instabilities while preserving positivity of density and internal energy under an explicit CFL condition. The second-order extension, based on WENO-type nodal gradients combinations, with additional slope and flux limiting, preserves this admissibility property at each iteration.

The same subface framework was used to discretize the scalar heat-conduction and vectorial viscous-stress diffusion operators, yielding symmetric positive definite global diffusion matrices. For the vectorial problem, a divergence-free correction to the constitutive law ensures invertibility and positive definiteness.

The Euler and diffusion schemes are coupled into a full Navier–Stokes solver through a point-implicit, matrix-free iterative method. The implicit treatment is admittedly basic—only the diagonal blocks of the diffusion Jacobian are retained—but it removes the stiffness associated with the diffusion operators on highly anisotropic meshes, making the method practical on production grids without explicit storage of the global matrix.

A systematic study of the rotated shear line on anisotropic Cartesian meshes provided a quantitative understanding of how each Riemann solver interacts with boundary-layer meshes. The analysis shows that the numerical diffusion of the multi-point scheme scales favorably with wall-normal refinement—the configuration encountered in boundary layers—but grows anomalously with tangential refinement on three-dimensional anisotropic meshes. The isotropic multi-point scheme, derived as a composite formulation that removes the area anisotropy from the nodal system, suppresses this pathology while preserving the favorable normal-refinement scaling.

These properties were assessed on two- and three-dimensional hypersonic configurations. On the half-cylinder at Mach 17.605, the isotropic multi-point scheme correctly predicted the wall heat flux on both quadrangular and hybrid quad/tri meshes, while the three-wave scheme failed to converge and the modified three-wave and two-wave schemes over-diffused. On the Atmospheric Re-entry Demonstrator at Mach 24, the isotropic multi-point scheme produced results in good agreement with the MISTRAL block-structured reference solution both on a block-structured hexahedral mesh, as well as on a fully unstructured hybrid tetrahedral one.

Several directions remain open for future work. The extension to low-Mach-number flow would broaden

the applicability of the scheme to mixed subsonic–supersonic configurations. A high-order extension of the subface-based framework would reduce mesh imprint on coarser grids and fully leverage the composite formulation. The coupling with thermodynamic non-equilibrium and ablation models is a natural next step for complete re-entry trajectory computations. Finally, the rotated shear-line analysis provides a quantitative indicator that could be used to study the impact of anisotropic mesh adaptation aimed at minimizing numerical heat-flux error in the boundary layer.

Acknowledgements

This work has been undertaken under the auspices of the LRC ANABASE, which is a joint research laboratory between Institut de Mathématiques de Bordeaux and CEA-CESTA devoted to the development of innovative numerical methods for the simulation of complex fluid flows.

References

[1] J.D. Anderson. *Hypersonic and high-temperature gas dynamics*. AIAA education series, 2006.

[2] G.V. Candler, P.K. Subbareddy, and J.M. Brock. Advances in Computational Fluid Dynamics for Hypersonic Flows. *Journal of Spacecraft and Rockets*, 52(1), 2015.

[3] A. Chan. *Innovative numerical schemes for 3D supersonic aerodynamics on unstructured mesh*. PhD thesis, Université de Bordeaux, 2022. Thèse de doctorat dirigée par R. Loubère et P.-H. Maire.

[4] V. Delmas, R. Loubère, and P.-H. Maire. A node conservative cell-centered finite volume method for solving multidimensional Euler equations over general unstructured grids. *J. Comput. Phys.*, 539(114246), 2025.

[5] V. Delmas. *Mise au point et développement de méthodes numériques innovantes pour la résolution des équations de Navier–Stokes 3D en régime hypersonique sur maillages hybrides*. PhD thesis, Université de Bordeaux, 2026. Thèse de doctorat dirigée par R. Loubère et P.-H. Maire.

[6] G. Gallice. Approximation numérique de systèmes hyperboliques non-linéaires conservatifs ou non-conservatifs, 2002. Habilitation à Diriger des Recherches, Université Bordeaux I.

[7] A. Harten, P.D. Lax, and B. van Leer. On upstream differencing and Godunov-type schemes for hyperbolic conservation laws. *SIAM Review*, 25(1):35–61, 1983.

[8] E.F. Toro, M. Spruce, and W. Speares. Restoration of the contact surface in the HLL-Riemann solver. *Shock Waves*, 4:25–34, 1994.

[9] Z. Shen, W. Yan, and G. Yuan. A robust and contact resolving Riemann solver on unstructured mesh, Part I: Euler method. *J. Comput. Phys.*, 327:523–542, 2016.

[10] J.J. Quirk. A contribution to the great Riemann solver debate. *Int. J. Numer. Meth. Fluids*, 18:555–574, 1994.

[11] P.-H. Maire, R. Abgrall, J. Breil, and J. Ovadia. A cell-centered Lagrangian scheme for two-dimensional compressible flow problems. *SIAM J. Sci. Comput.*, 29(4):1781–1824, 2007.

[12] L.I. Sedov. *Similarity and Dimensional Methods in Mechanics*. Academic Press, 1959.

[13] J.R. Kamm and F.X. Timmes. On efficient generation of numerically robust Sedov solutions. Technical Report LA-UR-07-2849, Los Alamos National Laboratory, 2007.

[14] J. Annaloro, S. Galera, P. Kärräng, Y. Préveraud, J.-L. Vérant, M. Spel, P. Van Hauwert, and P. Omaly. Space Debris Atmospheric Entry Prediction with Spacecraft-Oriented Tools. In *Proc. 7th European Conference on Space Debris*, 2017.

[15] C. Geuzaine and J.-F. Remacle. Gmsh: A 3-D finite element mesh generator with built-in pre- and post-processing facilities. *Int. J. Numer. Meth. Engng.*, 79(11):1309–1331, 2009.

[16] P. Jacq. *Finite Volume methods on unstructured grids for solving anisotropic heat transfer and compressible Navier-Stokes equations*. PhD thesis, Ecole Doctorale de Mathématiques et d'Informatique, Université de Bordeaux, 2014. Available at `https://theses.hal.science/tel-01136442`.

[17] P.-H. Maire. *Contribution to the numerical modeling of Inertial Confinement Fusion*. Habilitation à diriger des recherches, Université Bordeaux I, 2011.

[18] D.N. Arnold and R.S. Falk. A new mixed formulation for elasticity. *Numer. Math.*, 53:13–30, 1988.

[19] V. Delmas, R. Loubère, and P.-H. Maire. A nominally second-order cell-centered Finite Volume scheme for solving vectorial diffusion equations on general unstructured grids: Application to the compressible Navier–Stokes equations. Preprint, to be submitted to J. Comput. Phys., 2026.

[20] P.A. Gnoffo. An upwind-biased, point-implicit relaxation algorithm for viscous, compressible perfect-gas flows. Technical Report 2953, NASA Langley Research Center, 1990.

[21] P.R. Ess and C.B. Allen. Parallel computation of two-dimensional laminar inert and chemically reactive multi-species gas flows. *Int. J. Numer. Methods Heat Fluid Flow*, 15(3):228–256, 2005.

[22] P. Hoch. Nodal extension of approximate Riemann solvers and nonlinear high-order reconstruction for finite volume methods on unstructured polygonal and conical meshes: the homogeneous case. Technical report, CEA, 2022.

[23] X. Blanc, P. Hoch, and C. Lasuen. Composite finite volume schemes for the diffusion equation on unstructured meshes. *Comput. Math. Appl.*, 156:207–217, 2024.

[24] M. Boujoudar, E. Franck, P. Hoch, P. Paragot, C. Lasuen, and Y. Le Hénaff. A composite finite volume scheme for the Euler equations with source term on unstructured meshes. In *ESAIM: Proceedings and Surveys*, 2024.

[25] X. Blanc, V. Delmas, and P. Hoch. Asymptotic preserving schemes on conical unstructured 2D meshes. *Int. J. Numer. Meth. Fluids*, 93(8):2763–2802, 2021.

[26] NASA FUN3D Development Team. Hypersonic benchmarks. `https://fun3d.larc.nasa.gov/chapter-2.html\#hypersonic_benchmarks`, 2026. Accessed: 2026-01-29.

[27] R. Tech. Mistral. Commercial CFD software. `https://www.rtech.fr`.